Volume 19
Number 19
21 May 2023
Pages 3407–3528

Soft Matter

rsc.li/soft-matter-journal

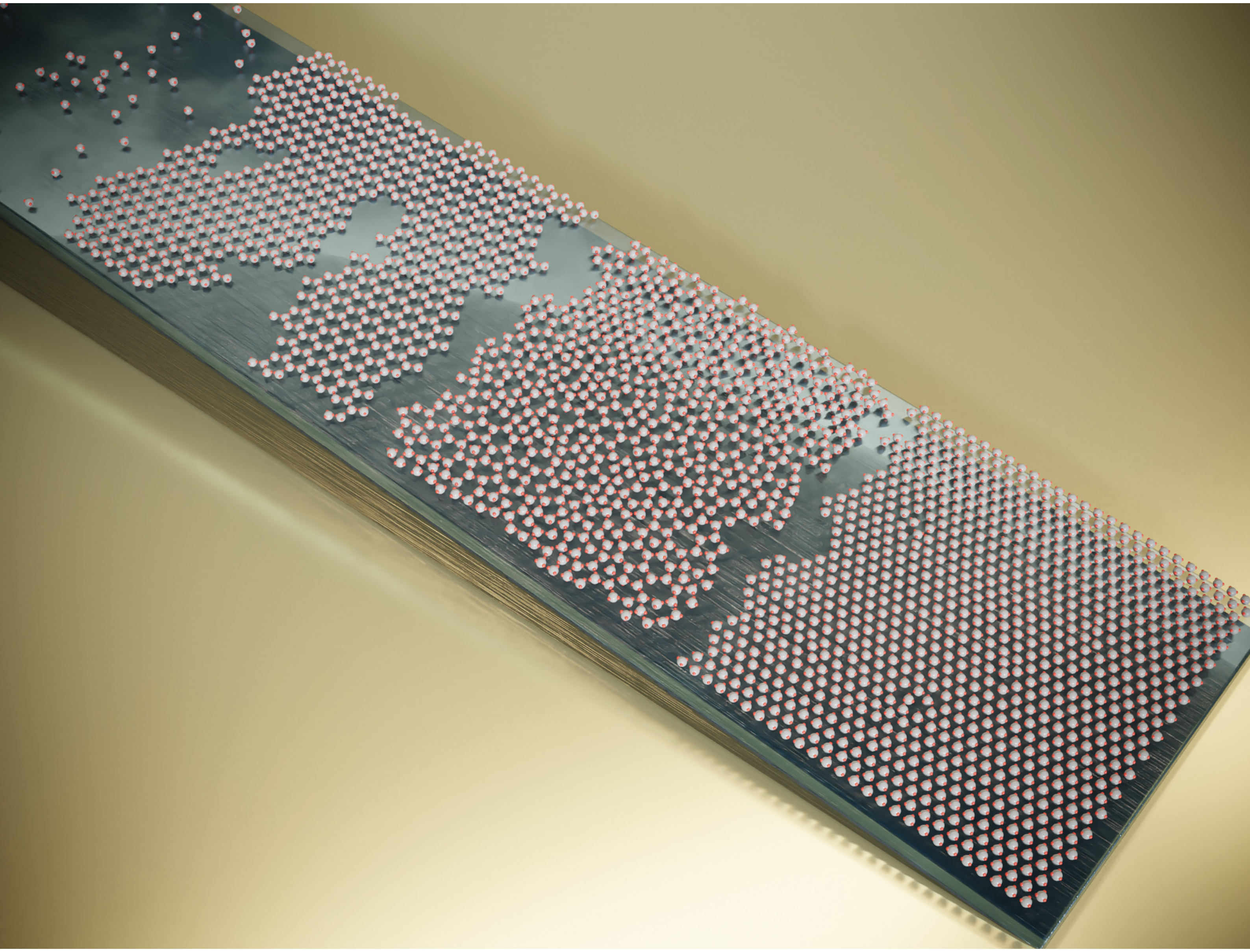

ISSN 1744-6848

ROYAL SOCIETY
OF **CHEMISTRY**

PAPER
Peter Schall *et al.*
Phases of surface-confined trivalent colloidal particles

Soft Matter

PAPER

View Article Online
View Journal | View Issue

Cite this: *Soft Matter*, 2023, **19**, 3414

Phases of surface-confined trivalent colloidal particles†

Piet J. M. Swinkels, [a] Zhe Gong, [b] Stefano Sacanna, [b] Eva G. Noya [c] and Peter Schall *[d]

Received 12th September 2022,
Accepted 6th April 2023

DOI: 10.1039/d2sm01237e

rsc.li/soft-matter-journal

Patchy colloids promise the design and modelling of complex materials, but the realization of equilibrium patchy particle structures remains challenging. Here, we assemble pseudo-trivalent particles and elucidate their phase behaviour when confined to a plane. We observe the honeycomb phase, as well as more complex amorphous network and triangular phases. Structural analysis performed on the three condensed phases reveals their shared structural motifs. Using a combined experimental and simulation approach, we elucidate the energetics of these phases and construct the phase diagram of this system, using order parameters to determine the phase coexistence lines. Our results reveal the rich phase behaviour that a relatively simple patchy particle system can display, and open the door to a larger joined simulation and experimental exploration of the full patchy-particle phase space.

I. Introduction

Colloidal particles are an ideal system for studying the assembly of complex materials. Despite their apparent simplicity, they can assemble into complex structures, sometimes even mimicking atomic materials, while still being easily studied using convenient light scattering or microscopy methods.[1] Modern synthesis methods can go far beyond the classic isotropic colloidal sphere, endowing particles with specific particle shape and valency to achieve higher complexity of assembled structures.[2–4] A subfield of colloidal assembly that has grown especially prominent over the past decade is the study of so-called patchy particles. These particles are decorated with patches of a material or surface affinity different from the bulk; the patches are typically used to induce specific attraction to other patches, and thus to steer the assembly towards specific phases.[5–7]

Simulations and experimental studies have revealed a wealth of structures that even relatively simple patch geometries can assemble into. Even one of the simplest possible cases – two-dimensional assembly of divalent particles – can lead to assembly of the complex kagome lattice.[6,8] Adding more patches leads to increasingly complex phase behaviour: tetravalent particles can assemble into a diamond lattice[9,10] – although with significant kinetic difficulties,[11] flexible patches or mixed patch numbers can lead to so-called "equilibrium gels",[12–14] and particles with 5 or 7 regularly arranged patches can assemble into 12-fold symmetrical quasicrystals.[15] The formed equilibrium structures do not only depend on particle geometry, but also on patch attractive strength and particle density.[11,16,17] Unfortunately, most of our knowledge about patchy particle assembly comes from simulations due to the challenge of realizing well-defined, reversibly assembling patchy particles and controlling their anisotropic interactions, making simulations the method of choice to elucidate their assembly and phase behaviour.[7]

However, recent advances in colloid chemistry and new experimental strategies are enabling the production of more complex particle geometries and the study of their equilibrium assembly in experiments.[18–21] Yet, experimental realization of reversible patch–patch bonding to produce equilibrium structures is still challenging, while it would open the door to many complex structures, analogues of atomic compounds and beyond.[22–24] One way to realize selective patch–patch attraction of tunable magnitude is through critical Casimir interactions that depend on the solvent affinity of the particle surfaces.[25–28] The critical Casimir force arises in binary solvents close to their critical point when the confinement of solvent fluctuations between the particle surfaces causes an effective attractive force on the order of the thermal energy, k_BT, tunable by the temperature offset ΔT from the solvent critical point, T_c.[29–31]

In experimental work on patchy particle systems, investigation of the complex phase behaviour has been rarely reported, with notable exceptions:[6,7,10,12] varying density and attractive strength is an added complexity of an already complex experimental system. Nevertheless, this is worthwhile, since the rich

---

[a] *Institute of Physics, University of Amsterdam, Amsterdam, The Netherlands*
[b] *Molecular Design Institute, Department of Chemistry, New York University, USA*
[c] *Instituto de Química-Física Rocasolano, CSIC, Madrid, Spain*
[d] *Institute of Physics, University of Amsterdam, Amsterdam, The Netherlands. E-mail: p.schall@uva.nl*

† Electronic supplementary information (ESI) available. See DOI: **https://doi.org/10.1039/d2sm01237e**

phase behaviour is one of the hallmarks of patchy particle systems, as highlighted by a range of simulations.[15,17,32–34]

Particular interest lies in tri-valent and tetra-valent particles as they promise to form phases analogous to those of carbon atoms: the graphene phase for the former, mimicking the sp^2 hybridized state of carbon atoms, and the diamond lattice for the latter, mimicking the sp^3 hybridized state.[10,16,32] Both structures are interesting candidates for photonic and phononic materials as they exhibit photonic and phononic band gaps.[22,35] Indeed, for trivalent particles, simulations have revealed a rich phase diagram, including besides the honeycomb lattice, also amorphous and triangular phases, but the experimental counterpart has remained elusive.[16]

Here, by finely tuning attractive patch–patch interactions in a system of pseudo-trivalent particles confined to a surface, we experimentally investigate their phase behaviour as a function of density and attraction. We employ critical Casimir forces in a near-critical binary solvent to adjust the patches' attractive strength on the scale of k_BT, the thermal energy, enabling us to reversibly and close to equilibrium explore the full range of the phase diagram. We observe the formation of three structurally distinct condensed phases: the honeycomb lattice, characterized by the hexagonal honeycomb motif, an amorphous network, characterized by pentagonal, hexagonal and heptagonal motifs, and the so-called triangular phase, a honeycomb lattice with the hexagon filled by an additional particle. These phases are confirmed in simulations performed at similar densities and attractive strengths. Using the local coordination number and characteristic lattice distance ratios as structural order parameters, we pinpoint the phase boundaries and compare with the simulation predictions. Our results reveal that simple surface-confined trivalent particles display a surprisingly complex phase diagram, highlighting the rich phase behaviour that even simple patchy particles can display. These results open the door to complex colloidal (*meta-*)materials, such as directionally bonded low-density crystals and amorphous networks, which have potential for phononic and photonic applications.[22,35]

II. Methods

We fabricate patchy particles from polystyrene (PS) and 3-(trimethoxysilyl)propyl methacrylate (TPM) spheres by colloidal fusion.[20] The synthesis yields particles with a PS bulk and tetrahedrally coordinated fluorescently labeled TPM patches (Fig. 1a and b). The particles have a diameter of σ = 2.0 μm and a patch diameter $d_p \approx$ 0.5 μm (see ESI†); the latter is sufficiently small to allow only single patches to bind with each other. To induce an effective patch–patch attraction of controllable magnitude, we suspend the particles in a binary solvent close to its critical point. The confinement of solvent fluctuations between the particle surfaces then causes attractive critical Casimir interactions on the order of the thermal energy, k_BT, tunable by the absorption preference of the patches and the temperature offset ΔT from the solvent coexistence temperature, T_{cx}.

We use a binary mixture of lutidine and water with lutidine volume fraction c_L = 0.25 close to the critical volume fraction

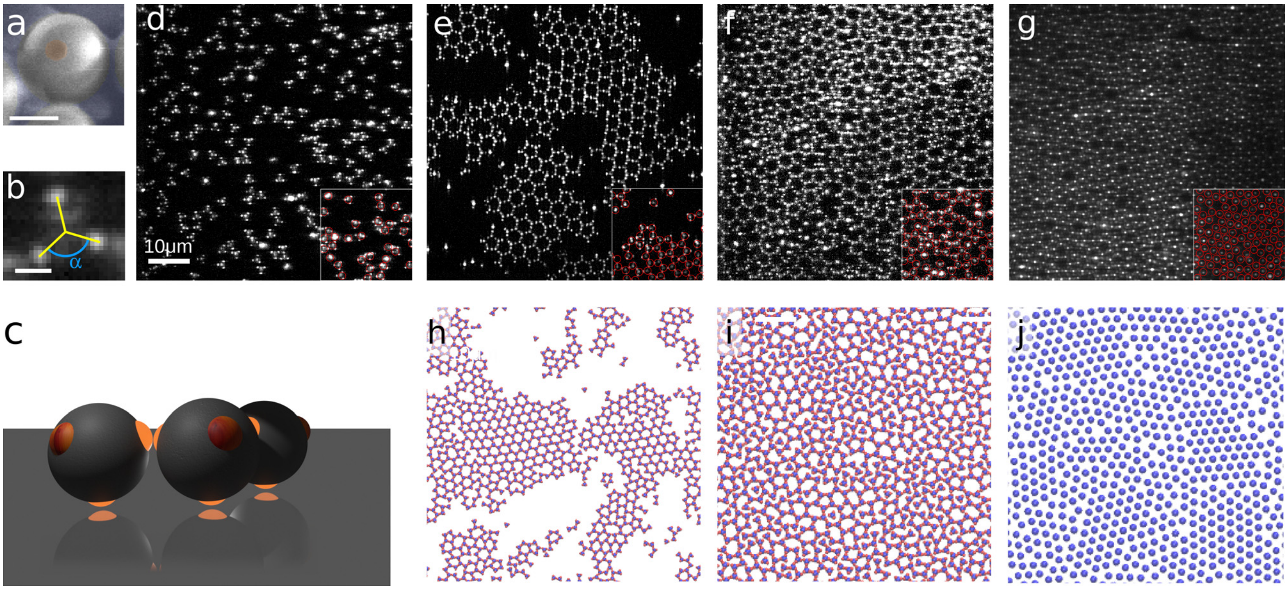

Fig. 1 Pseudo-trimeric tetrahedral particles and their phases: fluid, honeycomb, amorphous and triangular (a–c) tetrahedral particles become trivalent upon attachment of one patch to the substrate. (a) Scanning electron microscopy (SEM) image of a patchy particle with patch highlighted in orange. (b) Confocal microscope image of a particle taken under fluorescence. The projected angle between the patches is indicated by α, corresponding to 120°. The scale bar in both panels is 1 μm. (c) Reconstruction of surface-bound particles, exhibiting three remaining patches to bind to other particles. (d–g) Confocal microscopy images of experimentally observed phases: fluid (d), honeycomb-fluid coexistence (e), amorphous network (f), and triangular phase (g). Inset shows part of the image with particles superimposed in red. (h–j) Snapshots of the phases observed in the simulations, corresponding to the experimental phases in (d–g). In panel (j), the red patches are hidden to highlight the triangular packing of particles.

$c_{\mathrm{L,c}} = 0.27$,[36] and solvent demixing temperature $T_{\mathrm{cx}} = 33.95$ °C, and add 1 mM of $\mathrm{MgSO_4}$ to screen the particles' electrostatic repulsion and enhance the lutidine adsorption of the hydrophobic patches.[26] The suspension is injected into a glass capillary with hydrophobically treated walls (see ESI†) to which the particle patches bind and the particles become adsorbed *via* one of their patches at approx. $\Delta T \leq 0.7$ °C. The resulting pseudo-trivalent particles diffuse freely along the surface (see Note S1, ESI†), until at approx. $\Delta T \leq 0.45$ °C, the remaining free patches start attracting each other and structures start to form, as illustrated in Fig. 1c.

To study the formation of phases, we slowly approach T_{c} in steps of 0.01 °C or larger (up to 0.05 °C), starting from $\Delta T = 0.65$ °C. We tilt the sample cell slightly to induce a small particle density gradient, allowing us to study a range of particle area fractions η at a constant ΔT, see ESI.† Several regions in the sample along the density gradient are then imaged by confocal microscopy to locate both the particles' centre of mass and fluorescent patches, allowing us to determine the particles' bond angles with their neighbours (for tracking details, see ESI†). By focussing at different heights, we can accurately determine the horizontal position of the particle centre (from the glass-bound patch) and the bonds between particles (from the bonding patches).

We also perform Monte Carlo (MC) simulations to aid the mapping of the phases. The interaction between particles is set by a generalized Lennard-Jones (LJ) repulsive core and an attractive tail modulated by an angle-dependent function, which is a reasonable model for our patchy particle system.[37,38] Further simulation details are given in ESI.† Simulations are performed at a range of different reduced temperatures (T^*) and surface coverages. We calibrate the inter-particle potentials at several ΔT and T^* to be able to directly compare experiments and simulations at similar attractive strength (see Note S4, ESI†).

III. Results and discussion

A. Observation of honeycomb, amorphous network, and triangular phases

At low patch–patch interaction strength (high ΔT) and low area fraction ($\eta \lesssim 0.5$), the particles form a two-dimensional colloidal fluid, see Fig. 1d. By measuring the diffusion constant of the particles, we confirm that they can diffuse freely over the surface, see ESI.† When we increase the patch–patch interaction strength by decreasing ΔT to $\lesssim 0.38$ °C, the particles form flakes of honeycomb lattice coexisting with a dilute fluid phase, see Fig. 1e. In the lattice, each particle binds three other particles at 120° angle with respect to each other, resulting in the typical repeating 6-membered rings motif of the honeycomb lattice. The honeycomb lattice is common in nature and engineering at all length scales due to its extraordinary mechanical and electronic properties.[39,40] Famous examples include graphene, formed by the two-dimensional assembly of trivalent atoms.

At higher densities, more exotic structures emerge. At an area fraction of $\eta \sim 0.55$, an amorphous network is observed as shown in Fig. 1f. This network is characterized by a wide distribution of ring sizes, in which particles exhibit non-ideal bond angles, slightly above or below 120 °C. In this network, the open nature of the honeycomb lattice is preserved, but the order is lost: unlike in the honeycomb lattice, the rings do not periodically tile the surface but fill the plane seemingly without long-range order. As we applied the same slow increase of the attractive strength, at a density that is still low enough for rearrangement (far below random close packing), we believe this amorphous network to be an equilibrium phase. This is confirmed in our simulations that show a similar transition from the honeycomb lattice to the amorphous phase, albeit with small structural differences to the experimental one, as depicted in Fig. 1h and i. Such an equilibrium phase formed by limited valency particles has long been predicted by simulations and theory[14,41]

At yet higher densities, $\eta \gtrsim 0.6$, the particles pack tightly in the triangular phase, see Fig. 1g, where we focus on the surface-bound patches demarcating the particle centres to highlight the underlying structure: the particles are ordered in a dense hexagonal crystal, while still being bonded to their neighbours *via* their attractive patches. The triangular lattice can be regarded as a honeycomb structure with each honeycomb cell occupied by an additional particle, although the additional particles that fill the voids typically destroy the honeycomb bond network. This phase is likewise confirmed in the simulations, as shown by the snapshot in Fig. 1j. The simulations thus capture our experimental results very well: simulated and experimental snapshots display remarkably similar structures; the three condensed phases are formed both in experiment and simulation.

B. Structural analysis

To further elucidate the relation of the amorphous and triangular phases to the honeycomb lattice, we analyse their structures in more detail. Important structural motifs are the rings, whose sizes are characteristic of the phases: they are strictly 6-membered in the honeycomb lattice, and more broadly distributed in the amorphous phase.[16,32,42,43] Ring-size distributions of both phases are shown in Fig. 2a, where bars indicate experimental measurements and dots simulation results. Indeed, the honeycomb phase consists primarily of 6-membered rings as expected, while also showing a small fraction of 5- and 7-membered rings, which we associate with defects, mostly situated at grain boundaries, see Fig. 1e and h. The amorphous network phase, in contrast, displays a much broader distribution of ring sizes, indicating that this phase consists of a variety of motifs in its bulk, including large fractions of 5- and 7-membered rings. This broad ring-size distribution is a hallmark of two-dimensional trivalent particle networks: similar distributions have been found in amorphous silica and the theoretical triangle network, even though the bond details (bending and stretching strain) are very different from our case.[42] Comparison of the experimental and simulated ring-size distributions reveals an interesting effect: in experiments, the number of 5-membered rings is significantly larger than that of

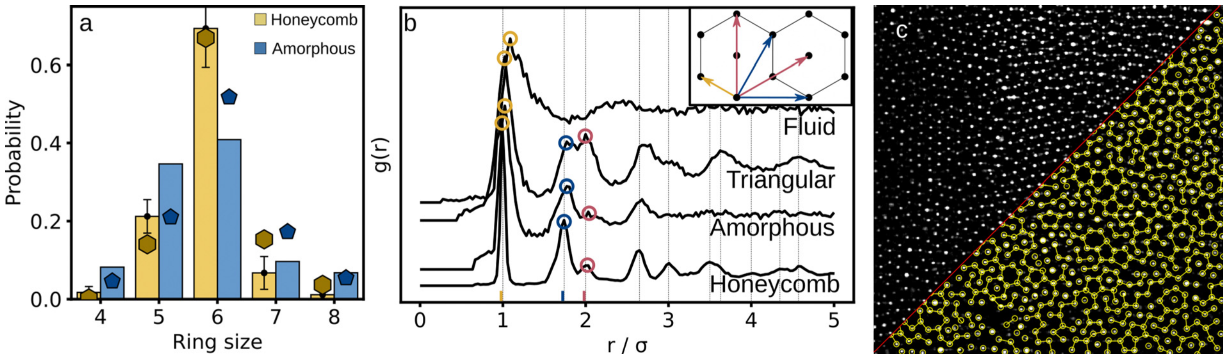

Fig. 2 Structural analysis. (a) Ring size distribution in the honeycomb phase (yellow, determined from 8 representative images) and amorphous phase (blue, determined from 2 representative images). The histogram shows experimental results, the dots the results from simulations. (b) Radial distribution function, $g(r)$ of the three different condensed phases, honeycomb (solid line), amorphous (dotted line), and triangular (dashed line). The $g(r)$ has been normalized to the height of its nearest-neighbour peak as well as shifted along the y-axis. The vertical dotted lines indicate theoretical peak locations, full analysis can be found in the ESI.† The inset shows a schematic drawing of the three smallest typical distances in our system, 1σ (yellow), 1.74σ (blue) and 2σ (red). The corresponding peaks in the $g(r)$ are highlighted. (c) Triangular lattice: confocal image and bonding network. The top-left half of the image shows the glass-bound patches, indicating the particle centres, while the bottom-right shows the overlaid bonding network where the patches and their bonds are highlighted in yellow.

the 7-membered rings, while in simulations, the distribution is more symmetric. This difference may originate from kinetic effects, favouring smaller ring sizes in the experiments, from the different effective patch sizes of experiments and simulations, or from many-body effects in experiments.

Further distinction of the amorphous and honeycomb phases can be made *via* the pair correlation function $g(r)$, plotted in Fig. 2b. At short distances, the $g(r)$ of the two phases is remarkably similar: all initial peaks coincide, indicating similar short-range distances, a direct result of their very similar basic structural motifs. Both phases consist of rings related to the particles' valency: hexagons in the honeycomb case, a mix of mainly penta-, hexa-, and heptagons in the amorphous case. These rings share similar typical internal distances, leading to similar short-range radial distribution functions (see ESI†). For the amorphous phase however, the peaks diminish after a few particle radii, as $g(r)$ decorrelates at larger distances because each shell of rings introduces a diverging number of ring-size combinations and associated characteristic distances. These effects are in line with other observations of amorphous networks consisting of trivalent subunits, and have been observed at length scales spanning from atomic to macroscopic.[42,44]

In contrast to the open honeycomb and amorphous phases, the triangular phase is characterized by a dense hexagonal crystal, giving rise to a dense network of patch–patch bonds. The bonds can be organized in a honeycomb lattice with particles in the voids, or as a disordered network of bonds.[16] In our case, we rather observe a disordered network of bonds, as shown by the split, annotated microscopic image in Fig. 2c, which illustrates the two layers of organization: triangular lattice (top left) and disordered bond network (bottom right). The glass-bound patches in the top-left demarcate the particle centres, clearly showing the dense hexagonal lattice of the phase. The bottom-right of the figure highlights the network of bonds between particles overlaid onto the image. Combined, both halves of Fig. 2c reveal the dense bonding network of the triangular phase. The structural relation to the honeycomb lattice is reflected in the $g(r)$ (Fig. 2b): the peak positions of the honeycomb and triangular lattices largely coincide, while the peak intensities differ significantly: for instance, the peaks corresponding to the second and third coordination shell at 1.74σ and 2.00σ respectively, have different relative heights (see Note S2, ESI†). In the honeycomb lattice there are six neighbours in the second coordination shell and three neighbours in the third coordination shell, while in the triangular phase there are six neighbours in each of these two coordination layers. The intensity ratio R of the two peaks in Fig. 2b thus characterizes open and closed phases: a ratio below 1 indicates an open structure (the honeycomb and amorphous phases), while a ratio above 1 corresponds to the closed triangular phase, see Note S4 (ESI†). Furthermore, in the absence of peaks, this ratio equals 1, signalling a low-density fluid phase.

C. Order parameters

Based on these structural properties, we can now define order parameters of the phases to pinpoint the coexistence lines and construct the phase diagram. In Fig. 3, we follow the main structural changes along lines of constant density and constant attraction and use the structural order parameters to determine the phase transition. The resulting experimental phase diagram is shown in Fig. 4a.

The fluid phase is characterized by a low number of bonded neighbours. Therefore, to pinpoint the fluid-honeycomb phase boundary, we determine the mean number of neighbours $\langle N_{\mathrm{nb}} \rangle$ of a particle as those with centres within 1.1σ of the particle under consideration. The resulting $\langle N_{\mathrm{nb}} \rangle$ as a function of η at two different interaction strengths (arrows 1 and 2 in Fig. 4a) is shown in Fig. 3a. In both cases, $\langle N_{\mathrm{nb}} \rangle \sim 0$ at low η, but jumps to $\langle N_{\mathrm{nb}} \rangle > 0$ and grows linearly with η at high η as a result of the growing fraction of the honeycomb phase in the fluid-honeycomb phase coexistence. This strong increase in $\langle N_{\mathrm{nb}} \rangle$ signals the transition from the low-density fluid to fluid-

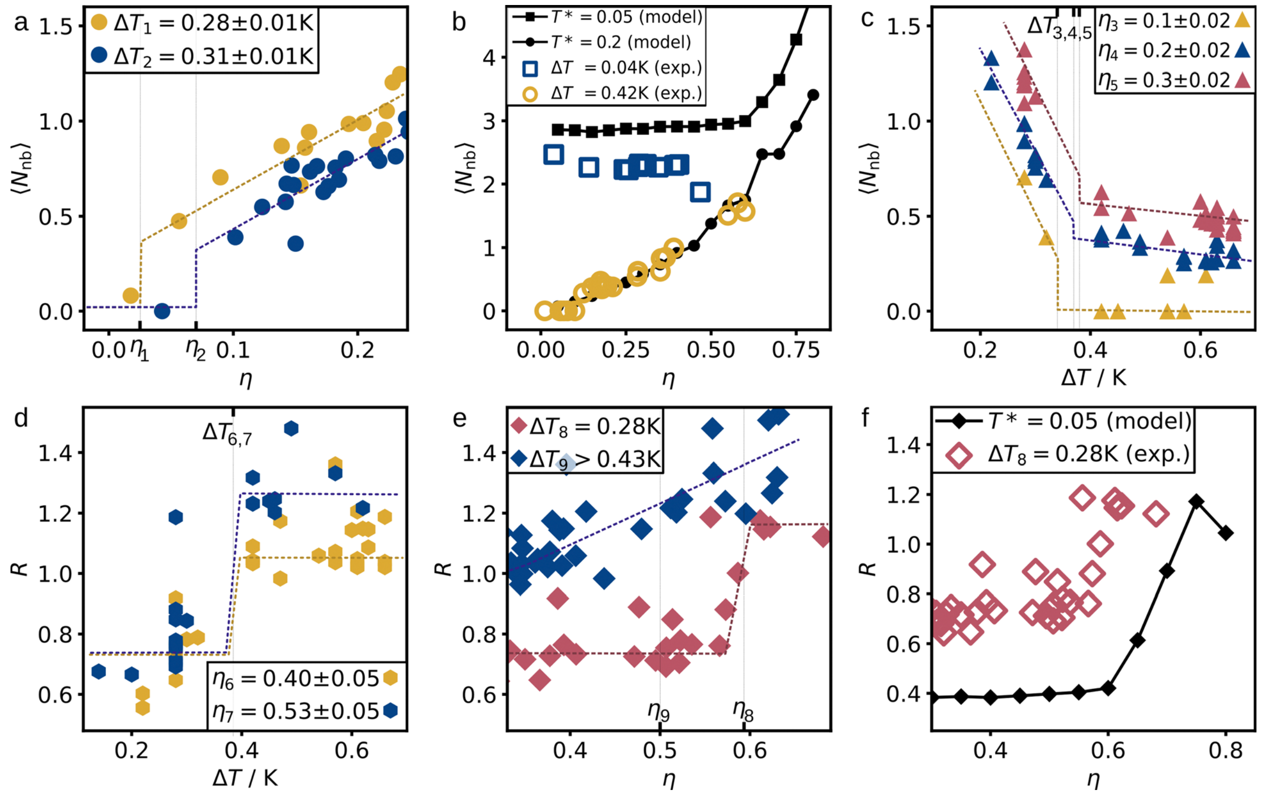

Fig. 3 Structural order parameters as a function of density and temperature. (a–c) Average number of neighbours $\langle N_{nb}\rangle$ as a function of surface coverage η (a and b) and ΔT (c). Panel (a) shows experimental data for two different attractive strengths (along arrows 1 and 2 in Fig. 4a, see legend), while (b) compares data from simulations in the fluid and honeycomb phase (black solid symbols and lines) with experimental data at corresponding attractive strength (coloured open symbols). Panel (c) shows $\langle N_{nb}\rangle$ as a function of ΔT for three densities (along arrows 3, 4 and 5 in Fig. 4a). (d–f) Height ratio R of characteristic $g(r)$ peaks as a function of ΔT (d) and η (e, f). Panel (d) shows R as a function of ΔT for two high surface coverages (arrows 6 and 7 in Fig. 4a.), while panels (e) and (f) show R as a function of η for experiments along arrows 8 and 9, and simulations at $T^* = 0.05$, respectively. The latter reveals good qualitative agreement of R in experiment and simulations. In all figure panels, dotted lines are guides to the eye.

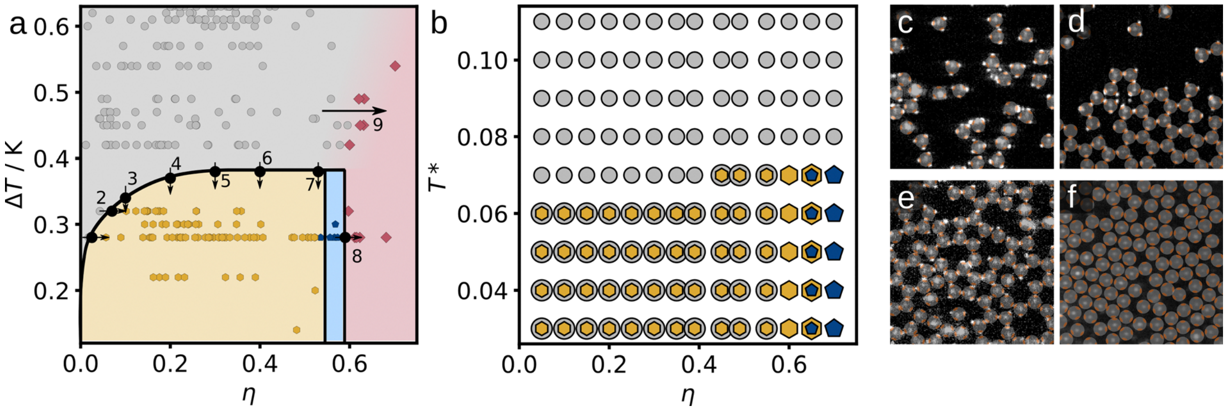

Fig. 4 Phase diagrams (a) Experimental phase diagram constructed from the order parameters in Fig. 3. The fluid phase is indicated in grey, the honeycomb-fluid coexistence in yellow, the amorphous network phase in blue and the triangular phase in red. Black arrows and dots indicate scans and estimated transitions shown in Fig. 3. (b) Corresponding phase diagram from simulations. Each point corresponds to a separate simulation. Gray circles indicate fluid, yellow hexagons indicate honeycomb, blue heptagons indicate amorphous network. Note that coexistence points have 2 symbols. (c–f) Illustrations of the experimentally observed phases: fluid (c), honeycomb-fluid coexistence (d), amorphous network (e) and triangular lattice (f). Here, patchy particle sketches are overlaid on small sections of confocal microscope images (insets of Fig. 1d–g) to illustrate the assembled structures most clearly.

honeycomb coexistence. The exact nature of the transition such as amount of supercooling, finite-size effects, *etc.* cannot be concluded from the current data, neither the exact location of the transition. The plotted dashed lines are therefore indicative only. At much lower attraction, $\langle N_{\mathrm{nb}}\rangle$ increases continuously with η, indicating the pure fluid phase, while at much higher attraction, $\langle N_{\mathrm{nb}}\rangle$ saturates at ~ 3, indicating the honeycomb phase, as consistently shown for experiments and simulations in Fig. 3b. The behaviour of experimental and numerical data is strikingly similar: the evolution of $\langle N_{\mathrm{nb}}\rangle$ in the fluid phase (at $T^* = 0.2$ and $\Delta T = 0.42$ °C) almost perfectly overlap, as may be expected from their similar attractive strength (Note S4, ESI†). In the honeycomb phase (at $T^* = 0.05$ and $\Delta T = 0.04$ °C), the trend is also similar, while the slightly lower $\langle N_{\mathrm{nb}}\rangle$ observed in experiments reflects the higher number of defects and surface particles lacking one bonding neighbour. At this interaction strength equivalent to $\sim 20k_{\mathrm{B}}T$, the fluid-honeycomb coexistence phase extends all the way to low density, resulting in the $\langle N_{\mathrm{nb}}\rangle$ plateaus.

We also explore the fluid-honeycomb transition along vertical lines in the phase diagram, by plotting the experimentally observed $\langle N_{\mathrm{nb}}\rangle$ as a function of ΔT for three different volume fractions (arrows 3, 4, and 5 in Fig. 4a) in Fig. 3c. At high ΔT (low attraction) the system is in the fluid phase and $\langle N_{\mathrm{nb}}\rangle$ is low. When the attraction increases towards smaller ΔT, $\langle N_{\mathrm{nb}}\rangle$ jumps and increases strongly, signalling the transition from the fluid phase to honeycomb-fluid coexistence. While the transitions cannot be pinpointed unambiguously from the experimental data, our simulations predict that the transition temperature ΔT increases, *i.e.* the attraction decreases for increasing density.

At higher density, $\langle N_{\mathrm{nb}}\rangle$ is no longer a good indicator of the phases. Instead, we can make use of the characteristic height ratio R of the $g(r)$ peaks at 1.74σ and 2.00σ as an order parameter of the phase transitions, as shown by the $g(r)$ curves in Fig. 2b. We exploit this ratio R for characterizing the transition from fluid and triangular phases to the honeycomb phase (along paths 6 and 7 in Fig. 4a) in Fig. 3d. Within each phase, we expect R to be constant due to the constant nearest-neighbour structure of each phase (neglecting the slight dependence of the fluid nearest neighbour structure on density). This is roughly displayed by the data, though firm conclusions are prohibited by the large spread of the data. Depending on the density, we observe different behaviour: at lower density $\eta_6 = 0.40$, R is approximately 1 at low interaction strength and drops to values lower than 1 at $\Delta T_6 \approx 0.35$ K, indicating a transition from the fluid phase to the honeycomb lattice. At higher density 0.53, in contrast, R adopts values larger than 1 at low interaction strength, and again transitions to values lower than 1 as interaction strength increases, indicating that the system undergoes a transition from the triangular to the honeycomb lattice, as shown in the phase diagram in Fig. 4a.

R is also a suitable order parameter to detect the transition from the amorphous to the triangular phase along arrows 8 and 9 in Fig. 4a. We follow it as a function of η at $\Delta T_8 = 0.28$ °C in Fig. 3e. The transition at $\eta_8 = 0.58$ indicates the phase transition from the open amorphous lattice to the triangular lattice. We note that there may be a small coexistence region as suggested by the fact that some of the rings in Fig. 1f and i are filled with a particle; we therefore indicate the jump of R more gradual, with a sloped line in Fig. 3e. The simulations show a similar transition from an open to a closed structure in Fig. 3f. The transition occurs at a slightly higher density compared to experiments, which is expected given the somewhat shifted phase diagram of the simulations. The difference in magnitude of R between simulation and experiment is probably due to the inherent noise present in the experimental data, leading to R values closer to $R = 1$. The evolution along path 9 at $\Delta T_9 > 0.43$ °C is more ambiguous. We notice a continuous slight increase in R, reflecting some degree of triangular ordering towards high density. At these low attractions, the phase behavior of the system should go over into that of hard spheres. More precisely, our particles are slightly charged, lowering transition densities with respect to those of hard spheres, but we expect qualitatively similar behavior. The rather continuous increase in triangular ordering indeed reminds of the continuous transition observed in 2D hard-sphere crystallization.[45]

IV. Discussion

The resulting density-temperature phase diagram for the experiments (Fig. 4a) shows the fluid phase indicated in grey, the honeycomb-fluid coexistence in yellow, the amorphous network phase in blue and the triangular phase in red. Each point in the diagram represents an observation. For comparison, the phase diagram from simulations is shown Fig. 4b. Illustrations of the observed phases based on experimental snapshots are shown in panels c–f.

The fluid phase present at high ΔT (low interaction strength) and low density consists of freely diffusing, non-bonded particles. The fluid-to-honeycomb transition occurs upon increasing interaction strength (decreasing ΔT) as indicated by arrows 3 to 6, and upon increasing density, along arrows 1 and 2. The phase transition from fluid-honeycomb coexistence to the amorphous phase takes place at surface coverage $\eta \sim 0.53$. The amorphous phase, while leaving part of the open honeycomb structure intact, packs particles at a higher density by introducing different ring sizes. This results in a structure, which is slightly denser than the honeycomb lattice, and contains only few unsaturated patches. Due to its open structure, the honeycomb lattice has a maximum packing fraction $\eta \approx 0.60$, beyond which the lattice simply cannot accommodate more particles, unless the lattice is deformed.[16] The amorphous network on the other hand can accommodate higher particle densities and has a higher configurational entropy, but pays an energy penalty for bending bonds out of their equilibrium angles to form non-ideal ring sizes. The balance between bending and bonding energies determines whether the amorphous network can be formed, and at what densities it is stable. Finally, the transition to the triangular phase is observed at area fraction $\eta \sim 0.6$, above which a dense packing of spheres is observed (Fig. 4f). Here, the particles are assembled in a dense hexagonal structure, with respective orientations such that as many patch–patch bonds as possible are formed. Nevertheless, even in a perfect triangular lattice, only

2 out of 3 patches can be bonded,[16] making this phase energetically unfavourable at lower densities.

At low interaction strength (high ΔT), experiments show a continuous increase in triangular ordering, indicated as a shaded transition from grey to red in Fig. 4. Simulations show a fluid phase up to about $\eta \lesssim 0.7$, fluid-triangular coexistence at $0.70 \lesssim \eta \lesssim 0.85$, and the triangular lattice at $\eta \gtrsim 0.85$. As the patches are only weakly attractive at such high ΔT, the particles interact mostly like isotropic colloids. At vanishingly low patch–patch interaction, the particles interact like hard spheres, which in two dimensions are expected to show continuous crystallization at packing fractions larger than $\eta \gtrsim 0.7$,[45–48] in agreement with the simulations. We hypothesize that the crystallization observed in experiments is akin to hard-sphere crystallization in 2D, but occurs at a somewhat lower density due to effective repulsions between the particles due to charging.[45]

The simulations show phase transitions at similar densities, albeit at systematically slightly higher values, which we attribute to the better equilibration of phases yielding slightly higher packing densities. The density of the pure honeycomb phase (at moderate temperature $T^* = 0.05$) is $\eta \sim 0.60$, consistent with the value obtained by setting the nearest-neighbour distance to that of the minimum of the potential. The density of the amorphous phase is $\eta \sim 0.65–0.70$, again higher than that of the honeycomb crystal, but still significantly lower than random close packing of spheres in a plane, $\eta_{\mathrm{cp}} = 0.84$,[49] allowing for sufficient rearrangements and equilibration of the Monte Carlo simulations.

Despite this difference, the phase diagram Fig. 4b is in good agreement with the experimental one: the fluid, honeycomb and amorphous and triangular phases are all present at similar attractive strength and densities. At the same time, there is an interesting characteristic difference between experimental and simulated phases: in contrast to the experiments, the simulations show a pure honeycomb lattice in a narrow region of phase space in addition to the fluid-honeycomb coexistence. Yet, this difference is not too surprising: due to the short range of the critical Casimir force (on the order of 0.01σ, see Note S6, ESI†), the pure honeycomb region is expected to be extremely narrow and easily missed. Furthermore, kinetic effects may quickly lead to the amorphous phase.

V. Conclusion

By utilizing the exquisite control over patch–patch attraction offered by the critical Casimir force, we experimentally explore the pressure-attraction phase diagram of pseudo-trivalent colloidal particles adsorbed at a substrate. The relatively simple particles display a surprisingly rich phase behaviour, not only assembling into the honeycomb lattice, but also into an amorphous network and a triangular phase at increasing particle density. The three condensed phases are structurally closely related, and by combining experiments with simulations, we find that a delicate balance between bending and bonding energies determine their interconversion. By following order parameters along isobars and isotherms, we construct the phase diagram of the system.

The exploration of the complex phase diagram illustrates the increasingly advanced control over patchy particle assembly, and opens the door to experimental investigation of the full phase space of the assembly of patchy particles with different valencies. The surprisingly rich assembly behaviour found in this simple patchy particle system hints at a wealth of interesting behaviours in more complex systems; there is a huge phase space to explore, while varying parameters such as density, attractive strength, particle geometry, and system dimensionality.

Author contributions

P. J. M. S., E. G. N. and P. S. conceived the study. P. J. M. S. performed the experiments and analysed the data. Z. G. and S. S. made the particles and helped with the system. P. J. M. S. and P. S. wrote the manuscript, with help from E. G. N. All authors discussed the data and reviewed the manuscript.

Conflicts of interest

There are no conflicts to declare.

Acknowledgements

P. S. acknowledges funding through Vici grant 680-47-615 from the Netherlands Organization for Scientific Research (NWO). S. S. acknowledges support from the NSF CAREER award DMR-1653465. E. G. N. acknowledges funding from Agencia Estatal de Investigación and Fondo Europeo de Desarrollo Regional (FEDER), Grant No PID2020-115722GB-C21.

References

1 J. Lyklema, Particulate Colloids, *Fundamentals of Interface and Colloid Science*, Elsevier, 2005, vol. 4.

2 J. Mewis and N. J. Wagner, Non-spherical particles, *Colloidal Suspension Rheology*, Cambridge Series in Chemical Engineering, Cambridge University Press, Cambridge, 2011, pp. 155–179.

3 Z. Luo and B. Liu, Shape-Tunable Colloids from Structured Liquid Droplet Templates, *Angew. Chem.*, 2018, **130**(18), 5034–5039.

4 C. Chen, L. Xie and Y. Wang, Recent advances in the synthesis and applications of anisotropic carbon and silica-based nanoparticles, *Nano Res.*, 2019, **12**(6), 1267–1278.

5 Z. Zhang and S. C. Glotzer, Self-Assembly of Patchy Particles, *Nano Lett.*, 2004, **4**(8), 1407–1413.

6 Q. Chen, S. C. Bae and S. Granick, Directed self-assembly of a colloidal kagome lattice, *Nature*, 2011, **469**(7330), 381–384.

7 M. Liu and X. Zheng, Veronica Grebe, David J. Pine, and Marcus Weck. Tunable assembly of hybrid colloids induced by regioselective depletion, *Nat. Mater.*, 2020, 1–8.

8 F. Romano and F. Sciortino, Two dimensional assembly of triblock Janus particles into crystal phases in the two bond per patch limit, *Soft Matter*, 2011, **7**(12), 5799–5804.
9 Z. Zhang, A. S. Keys, T. Chen and S. C. Glotzer, Self-assembly of patchy particles into diamond structures through molecular mimicry, *Langmuir*, 2005, **21**(25), 11547–11551.
10 M. He, J. P. Gales, É. Ducrot, Z. Gong, G.-R. Yi, S. Sacanna and D. J. Pine, Colloidal diamond, *Nature*, 2020, **585**(7826), 524–529.
11 E. G. Noya, I. Zubieta, D. J. Pine and F. Sciortino, Assembly of clathrates from tetrahedral patchy colloids with narrow patches, *J. Chem. Phys.*, 2019, **151**(9), 094502.
12 S. Biffi, R. Cerbino, F. Bomboi, E. M. Paraboschi, R. Asselta, F. Sciortino and T. Bellini, Phase behavior and critical activated dynamics of limited-valence DNA nanostars, *Proc. Natl. Acad. Sci. U. S. A.*, 2013, **110**(39), 15633–15637.
13 E. Lattuada, D. Caprara, R. Piazza and F. Sciortino, Spatially uniform dynamics in equilibrium colloidal gels, *Sci. Adv.*, 2021, **7**(49), eabk2360.
14 E. Bianchi, J. Largo, P. Tartaglia, E. Zaccarelli and F. Sciortino, Phase Diagram of Patchy Colloids: Towards Empty Liquids, *Phys. Rev. Lett.*, 2006, **97**(16), 168301.
15 M. N. van der Linden, J. P. K. Doye and A. A. Louis, Formation of dodecagonal quasicrystals in two-dimensional systems of patchy particles, *J. Chem. Phys.*, 2012, **136**(5), 054904.
16 E. G. Noya, N. G. Almarza and E. Lomba, Assembly of trivalent particles under confinement: From an exotic solid phase to a liquid phase at low temperature, *Soft Matter*, 2017, **13**(17), 3221–3229.
17 H. Eslami, K. Bahri and F. Müller-Plathe, Solid–Liquid and Solid–Solid Phase Diagrams of Self-Assembled Triblock Janus Nanoparticles from Solution, *J. Phys. Chem. C*, 2018, **122**(16), 9235–9244.
18 V. Meester, R. W. Verweij, C. Van Der Wel and D. J. Kraft, Colloidal Recycling: Reconfiguration of Random Aggregates into Patchy Particles, *ACS Nano*, 2016, **10**(4), 4322–4329.
19 R. M. Choueiri, E. Galati, H. Thérien-Aubin, A. Klinkova, E. M. Larin, A. Querejeta-Fernández, L. Han, H. L. Xin, O. Gang, E. B. Zhulina, M. Rubinstein and E. Kumacheva, Surface patterning of nanoparticles with polymer patches, *Nature*, 2016, **538**(7623), 79–83.
20 Z. Gong, T. Hueckel, G. R. Yi and S. Sacanna, Patchy particles made by colloidal fusion, *Nature*, 2017, **550**(7675), 234–238.
21 E. Duguet, E. Ducrot and S. Ravaine, Colloidal Molecules and Colloidal Polymers, *Functional Materials from Colloidal Self-Assembly*, John Wiley & Sons, Ltd, 2022, ch. 1, pp. 1–36.
22 J. H. Lee, J. P. Singer and E. L. Thomas, Micro-/nanostructured mechanical metamaterials, *Adv. Mater.*, 2012, **24**(36), 4782–4810.
23 J.-H. Huh, K. Kim, E. Im, J. Lee, Y. D. Cho and S. Lee, Exploiting Colloidal Metamaterials for Achieving Unnatural Optical Refractions, *Adv. Mater.*, 2020, **32**(51), 2001806.
24 T. Hueckel, G. M. Hocky and S. Sacanna, Total synthesis of colloidal matter, *Nat. Rev. Mater.*, 2021, **6**(11), 1053–1069.
25 T. A. Nguyen, A. C. Newton, S. J. Veen, D. J. Kraft, P. G. Bolhuis and P. Schall, Switching colloidal superstructures by critical casimir forces, *Adv. Mater.*, 2017, **29**(34), 1–6.
26 P. J. M. Swinkels, S. G. Stuij, Z. Gong, H. Jonas, N. Ruffino, B. van der Linden, P. G. Bolhuis, S. Sacanna, S. Woutersen and P. Schall, Revealing pseudorotation and ring-opening reactions in colloidal organic molecules, *Nat. Commun.*, 2021, **12**(1), 2810.
27 I. A. Martínez, C. Devailly, A. Petrosyan and S. Ciliberto, Energy Transfer between Colloids via Critical Interactions, *Entropy*, 2017, **19**(2), 77.
28 L. Helden, T. Knippenberg, L. Tian, A. Archambault, F. Ginot and C. Bechinger, Critical Casimir interactions of colloids in micellar critical solutions, *Soft Matter*, 2021, **17**(10), 2737–2741.
29 C. Hertlein, L. Helden, A. Gambassi, S. Dietrich and C. Bechinger, Direct measurement of critical Casimir forces, *Nature*, 2008, **451**(7175), 172–175.
30 A. Gambassi, A. Maciołek, C. Hertlein, U. Nellen, L. Helden, C. Bechinger and S. Dietrich, Critical Casimir effect in classical binary liquid mixtures, *Phys. Rev. E*, 2009, **80**(6), 061143.
31 S. G. Stuij, M. Labbé-Laurent, T. E. Kodger, A. Maciołek and P. Schall, Critical Casimir interactions between colloids around the critical point of binary solvents, *Soft Matter*, 2017, **13**(31), 5233–5249.
32 G. Doppelbauer, E. Bianchi and G. Kahl, Self-assembly scenarios of patchy colloidal particles in two dimensions, *J. Phys.: Condens. Matter*, 2010, **22**(10), 104105.
33 F. Romano, E. Sanz, P. Tartaglia and F. Sciortino, Phase diagram of trivalent and pentavalent patchy particles, *J. Phys.: Condens. Matter*, 2012, **24**(6), 064113.
34 D. Zeb Rocklin and X. Mao, Self-assembly of three-dimensional open structures using patchy colloidal particles, *Soft Matter*, 2014, **10**(38), 7569–7576.
35 D. Liu, Y. Gao, A. Tong and S. Hu, Absolute photonic band gap in 2D honeycomb annular photonic crystals, *Phys. Lett. A*, 2015, **379**(3), 214–217.
36 S. Z. Mirzaev, R. Behrends, T. Heimburg, J. Haller and U. Kaatze, Critical behavior of 2,6-dimethylpyridine-water: Measurements of specific heat, dynamic light scattering, and shear viscosity, *J. Chem. Phys.*, 2006, **124**(14), 144517.
37 J. P. K. Doye, A. A. Louis, I.-C. Lin, L. R. Allen, E. G. Noya, A. W. Wilber, H. C. Kok and R. Lyus, Controlling crystallization and its absence: Proteins, colloids and patchy models, *Phys. Chem. Chem. Phys.*, 2007, **9**, 2197–2205.
38 E. G. Noya, C. Vega, J. P. K. Doye and A. A. Louis, The stability of a crystal with diamond structure for patchy particles with tetrahedral symmetry, *J. Chem. Phys.*, 2010, **132**, 234511.
39 Q. Zhang, X. Yang, P. Li, G. Huang, S. Feng, C. Shen, B. Han, X. Zhang, F. Jin, F. Xu and T. J. Lu, Bioinspired engineering of honeycomb structure – Using nature to inspire human innovation, *Prog. Mater. Sci.*, 2015, **74**, 332–400.
40 D. Akinwande, C. J. Brennan, J. S. Bunch, P. Egberts, J. R. Felts, H. Gao, R. Huang, J.-S. Kim, T. Li, Y. Li,

K. M. Liechti, N. Lu, H. S. Park, E. J. Reed, P. Wang, B. I. Yakobson, T. Zhang, Y.-W. Zhang, Y. Zhou and Y. Zhu, A review on mechanics and mechanical properties of 2D materials—Graphene and beyond, *Extreme Mech. Lett.*, 2017, **13**, 42–77.

41 E. Zaccarelli, S. V. Buldyrev, E. La Nave, A. J. Moreno, I. Saika-Voivod, F. Sciortino and P. Tartaglia, Model for Reversible Colloidal Gelation, *Phys. Rev. Lett.*, 2005, **94**(21), 218301.

42 C. Büchner, P. Schlexer, L. Lichtenstein, S. Stuckenholz, M. Heyde and H.-J. Freund, Topological Investigation of Two-Dimensional Amorphous Materials, *Z. Phys. Chem.*, 2014, **228**(4–5), 587–607.

43 A. Kumar, D. Sherrington, M. Wilson and M. F. Thorpe, Ring statistics of silica bilayers, *J. Phys.: Condens. Matter*, 2014, **26**(39), 395401.

44 C. Büchner, L. Liu, S. Stuckenholz, K. M. Burson, L. Lichtenstein, M. Heyde, H.-J. Gao and H.-J. Freund, Building block analysis of 2D amorphous networks reveals medium range correlation, *J. Non-Cryst. Solids*, 2016, **435**, 40–47.

45 U. Gasser, Crystallization in three- and two-dimensional colloidal suspensions, *J. Phys.: Condens. Matter*, 2009, **21**(20), 203101.

46 M. A. Bates and D. Frenkel, Influence of vacancies on the melting transition of hard disks in two dimensions, *Phys. Rev. E*, 2000, **61**(5), 5223–5227.

47 S. Pronk and D. Frenkel, Melting of polydisperse hard disks, *Phys. Rev. E*, 2004, **69**(6), 066123.

48 E. P. Bernard and W. Krauth, Two-Step Melting in Two Dimensions: First-Order Liquid-Hexatic Transition, *Phys. Rev. Lett.*, 2011, **107**(15), 155704.

49 M. Sperl, J. Zhang, T. S. Majmudar and R. P. Behringer, Jamming for a 2d granular material, *Soft Matter*, 2010, **6**, 2982–2991.